Quantitative analysis of sheared unsaturated wet granular materials using X-ray micro-tomography and advanced segmentation techniques

Ahmad Awdi, Camille Chateau, Abdoulaye Fall, Jean-Noël Roux, Patrick Aimedieu

Quantitative Analysis of Sheared Unsaturated Wet Granular Materials Using X-ray Micro-tomography and Advanced Segmentation Techniques

Ahmad Awdi[a], Camille Chateau[a,1], Abdoulaye Fall[a], Jean-Noël Roux[a], Patrick Aimedieu[a]

[a]Laboratoire Navier, Univ Gustave Eiffel, ENPC, Institut Polytechnique de Paris, CNRS, Marne-la-Vallée, France.
[1]To whom correspondence should be addressed. E-mail: camille.chateau@enpc.fr.

Abstract

The microstructure of sheared unsaturated wet granular materials, comprising solid particles, liquid phases, and void spaces, is explored using X-ray micro-tomography. Advanced segmentation techniques are employed to overcome challenges in distinguishing phases within the material, utilizing a combination of Random Forest and U-Net models for accurate segmentation of the X-ray images. This methodology enables the quantification of the solid and liquid fractions within the sample, revealing the effects of shear deformation on their distribution. Additionally, an automated tool is designed to characterize the local geometry of small liquid domains, classified according to the number of connected liquid bridges joining grain pairs and the shape of such clusters. It is shown that deformation redistributes the liquid phase, which tends to be excluded from the strongly sheared regions. Coordination number estimates agree with published numerical simulation results. The study also addresses some limitations related to voxel size. The robust tools to analyse complex three-phase microstructure of wet granular materials are expected to improve the modeling of their rheology under different conditions.

Keywords: X-ray micro-tomography, unsaturated wet granular materials, image segmentation, deep learning, microstructure characterization

Notice: This version of the article has been accepted for publication , after peer review but is not the Version of Record and does not reflect post-acceptance improvements , or any corrections. The Version of Record is available online at:
http://dx.doi.org/10.1007/s10035-025-01518-7

1 Introduction

Unsaturated wet granular materials exhibit an intricate microstructure composed of solid particles, liquid phases, and void spaces. Understanding their morphological and rheological characteristics is essential for various applications to geotechnical engineering, environmental science or process engineering. However, the flow behavior of these materials remains poorly understood due to their inherent complexity, which is compounded by the challenges of experimental instrumentation and the absence of unified theoretical frameworks. The degree of liquid wetting on the grains significantly influences their behavior, with even a small amount of liquid inducing cohesion through surface tension [1, 2].

Although the development of models for wet granular materials is still in its early stages, there has been a growing interest in recent years [1, 3–13]. The rheological behavior of these materials is strongly influenced by the interaction between the liquid and the grains, with its sensitivity depending on the level of saturation and the morphology of the liquid phase [14, 15]. It is well understood that introducing a small amount of liquid into a granular medium imparts cohesive properties due to the surface tension of the wetting liquid, which forms pendular bridges that attract neighboring grains. This particular combination, known as unsaturated wet granular material, can exhibit solid-like behavior, enabling phenomena such as the construction of sandcastles, which is not possible with dry sand that cannot maintain stability under gravity when slopes are steeper than the angle of repose [16, 17]. Four fundamental states of wet granular material are typically distinguished as the morphology of the three-phase mixture changes with varying liquid content [1, 2]: the pendular state, characterized by liquid bridges joining grains in contact or separated by a small distance; the funicular state, which includes both liquid bridges and liquid-filled pores; the capillary state, where almost all pores are filled with liquid, surface tension's contribution vanishes, but capillary suction pressure remains significant [18]; and the slurry state, where grains are entirely immersed and capillary action is absent.

Shearing unsaturated wet granular materials can lead to the redistribution of the wetting liquid, which, in turn, can change the bulk behavior of the material [3]. However, experimental studies on granular flows are challenging because of the opaque nature of these materials. Despite these challenges, significant insight have been gained through techniques, including Magnetic Resonance Imaging [19–22], digital imaging [23], Particle Image Velocimetry used in quasi-2D granular flows [24], and Particle Tracking Velocimetry [25]. However, these methods have limitations, including the need for sample preparation, lack of 3D resolution, or limited access to internal structure. X-ray micro-tomography provides high-resolution 3D images of the internal structure of materials without the need for destructive sample preparation, making it a valuable tool for studying the microstructure of unsaturated wet granular materials. This technique has been used in various studies [15, 26–32]. For instance, Manahiloh and Meehan [29] demonstrated how X-ray CT can be used in a suction-controlled environment to derive the soil water characteristic curve and measure interfacial contact angles in unsaturated granular media. Milatz et al. [31] used X-ray CT to analyze water retention behavior during cyclic drainage and imbibition, identifying direct relationships between capillary state variables—such as interfacial

areas and contact angles—and macroscopic water retention curves, which are critical for understanding the hydro-mechanical response of granular soils. Similarly, Milatz et al. [30] investigated the evolution of grain-scale features, including water clusters and interfacial areas, during uniaxial compression tests, revealing how suction-dependent volumetric responses and shear strength are influenced by capillary phenomena. Kido and Higo [32] extended this understanding by employing triaxial compression tests with X-ray micro-tomography to examine the role of liquid bridges and air-water interfacial curvature in the macroscopic behavior of dense sand. These studies collectively emphasize the pivotal role of capillary effects in linking pore-scale dynamics to macroscopic mechanical responses in granular systems. Additionally, Scheel et al. [15] demonstrated significant morphological changes in liquid structures as liquid content increased, highlighting the transition from liquid bridges and small morphologies into larger clusters. This transition indicates liquid redistribution within the granular pile and a corresponding increase in mechanical strength, which eventually plateaus as liquid bridges merge into larger clusters. According to Karmakar et al. [28], during shear cycles, liquid redistributes dynamically between different liquid morphologies. This redistribution is driven by pressure differences, where smaller liquid structures tend to receive liquid from larger ones through a volume-exchange process. As shear forces are applied, this continuous redistribution plays a crucial role in maintaining the stability of the wet granular assembly, despite the constant reorganization of the internal liquid network. Similarly, Badetti et al. [27] showed that shear deformation leads to a reduction in large liquid morphologies and an increase in capillary bridges, attributed to the motion of grains and liquid redistribution to neighboring contacts after the steady rupture of large clusters [33].

Previous methodologies, although groundbreaking, were limited in their ability to accurately and quantitatively characterize the complex liquid structures within wet granular materials. The lack of automated tools for precisely classifying liquid morphologies and quantifying their volumes and distributions has hindered a deeper understanding of how these structures influence rheological properties. In this paper, we aim at providing novel quantitative data on the distribution and evolution of liquid morphologies under shear using a model material.

Hence, we present a method to investigate the relationship between liquid morphology and material rheology. This approach utilizes a custom-built rheometer designed for insertion into an X-ray micro-tomograph, enabling in-situ rheometry experiments. The paper is organized in three sections. Section 2 details the materials used and the experimental procedures. Section 3 introduces the image segmentation method, employing machine learning and deep learning models. In Section 4, quantitative microstructure analysis tools are presented, providing access to local solid and liquid distributions, an automatic classification of liquid morphologies based on their geometry and the number of grains involved, and information on coordination numbers.

2 Experimental Procedures

The study was carried out on a model material composed of an assembly of uniformly sized polystyrene beads, with average diameter $d_p = 580\mu m$ and a standard deviation of 5% (sufficient to prevent crystallization), and a density $\rho_s = 1.05 g/cm^3$. Polystyrene was chosen due to its transparency to X-rays, which ensures high-quality imaging, and its low density, which minimizes gravity-induced effects. Given that polystyrene is a plastic material, potential electrostatic charging and adhesion effects may arise, particularly in the dry case. Such electrostatic effects are negligible in the investigated wet state. The beads are mixed and coated with a high-viscosity silicone oil with a viscosity of $\eta_f = 1093$ mPa.s at a temperature of $20°C$. The silicone oil has density $\rho_l = 0.95 g/cm^3$ and surface tension $\Gamma = 20.6$ mN/m. A high viscosity was chosen to ensure that the sample microstructure is stable with time. The wetting angle θ is very small, estimated to 5 degrees, and thus (with $\cos\theta \simeq 0.996$) one may assume perfect wetting for all practical purposes [34]. Furthermore, the amount of oil used in the experiments is quantified by the ratio of liquid volume V_L to solid volume V_S, expressed as $\epsilon = V_L/V_S = \phi_L/\phi_S = 0.05$, where ϕ_L and ϕ_S stand for the liquid and solid volume fractions, respectively. The samples are prepared by slowly adding the liquid to the polystyrene beads while manually and continuously mixing until a uniform mixture is achieved.

To image the evolution of the microstructure under shear, we designed and built a shear device, which can be inserted into the X-ray micro-tomograph imager (Figure 1a). A rheometer was selected as shearing device, as part of a broader effort to link microstructural changes in unsaturated wet granular materials to their macroscopic rheological behavior, including effects of viscosity. In practice, the sample is placed inside a cylindrical shear cell, made of polymethyl methacrylate (PMMA) (see Figure 1b). The cylindrical shear cell is centered by using a home-made centering set up, so that the axis of rotation of the shear cell is aligned with the axis of rotation of the rotating stage of the shear device, to ensure that the normal force and the rotation speed are precisely applied to the sample during the shear experiment. Initially the material is filled and compacted by imposing a normal force (applied by the weight of the upper plate, see Figure 1b), and then by manually tapping on the outer surface of the sample container to ensure a better filling of the shear cell. The sample reaches global packing fraction $\phi \approx 0.6$. Its dimensions are: diameter $D = 20$ mm and height $H = 10$ mm. It is important to note that the sample, once shear flow is driven by the stage rotation, can either dilate or compact. Instead of staying fixed, the gap size varies, maintaining a constant value of the imposed normal force [13, 27, 35, 36]. In the present experiment, the normal force is simply the weight of the PMMA upper plate (of mass $16.6g$, see Figure 1b). Reduced pressure P^* is defined [4, 27, 34], under confining stress σ_n, as the ratio of the typical grain-levelconfining force, $d_p^2\sigma_n$, to cohesive force F_0. Here σ_n is due to the weight of the upper plate (see Figure 1b), while one has $F_0 = \pi\Gamma d_p$, for grains of diameter d_p joined by menisci with surface tension Γ, assuming perfect wetting, resulting in $P^* = 4.1$.

The rotation of the upper plate is blocked by a set of carbon rods. The use of vertical rods minimizes the absorption of X-rays by the device, enabling a lower photo energy to be used to improve image contrast.

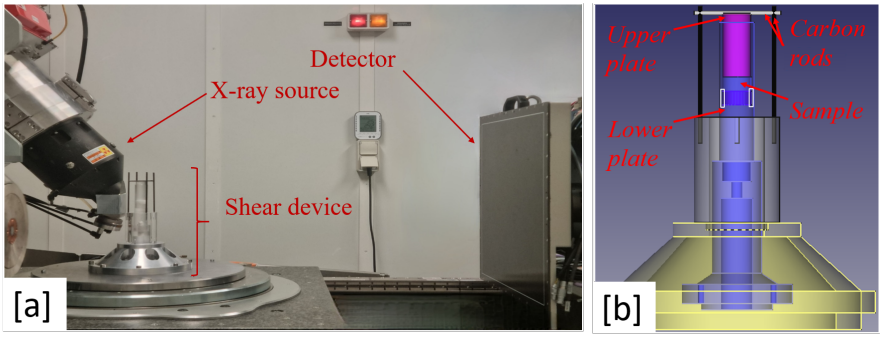

Fig. 1 Photograph [a] of the X-ray imaging experiment.The rotation and centering system is located under the stage of the tomograph, as shown in the sketch [b] of the confined shear plate-cup geometry.

Our laboratory is equipped with an X-ray micro-tomograph (Ultratom model, RX Solutions brand), which, when combined with our custom-made device, enables the acquisition of 3D images of the sheared material.

Initially, a tomography scan of the compacted state under reduced pressure P^*, serving as the reference sample for subsequent measurements, is performed. The material, after a preshear step in which the bottom plate is subjected to two full rotations ($720°$) at the rate of $10°/s$, is then prepared with the internal structure corresponding to a constant, small shear rate. We define the average shear rate $\dot{\gamma}$ from rotation angle θ by considering the shear strain in the middle of the region defined in terms of radial coordinate r by $0.45R \leq r \leq 0.9R$. The angular velocity corresponding to value $\dot{\gamma} = 8.48$ s^{-1} is maintained constant for 2 minutes. This corresponds to a rather large strain ($\gamma \simeq 1020$).

Whether shear rate $\dot{\gamma}$ is to be regarded as small, close to the quasistatic limit, depends on inertial and viscous effects. The *inertial number*, as introduced 20 years ago [37, 38], with definition $I = \dot{\gamma} d_p / \sqrt{\sigma_n / \rho_p}$, is the ratio of a characteristic inertial rearrangement time to shear time $1/\dot{\gamma}$, and conveniently characterizes inertial effects in shear flow under normal stress σ_n, as the unique relevant state variable if the stress level does not entail very large contact deflections in the granular material. Its value in the experiments reported here, about 7.10^{-3} are small enough for inertial effects to be quite small. However, viscous effects should also be assessed, and they are characterized by the value of the *viscous number* $I_v = \eta_s \dot{\gamma} / \sigma_n$ (see [34] and references therein). Its value in the present case, about 2.10^{-2}, is such that the microstructure might slightly, but notably differ from the one corresponding to quasistatic shear [34], in particular with a small density change (a decrease in Φ_S not exceeding 0.01). After 2 minutes the flow is stopped, and a new image acquisition is carried out. It is assumed that, due to the large viscosity of the liquid coating the grains, no significant structural change takes place while the tomographic signal is acquired.

These steps are repeated until a total shearing time of 10 minutes is reached.

The 3D images are acquired using a Varex 4343 DX-I imager (for each projection: 3032 x 3032 pixels, pixel pitch is 139 microns) and the X-ray source Hamamatsu L10801 (maximum voltage: 230 kV). For the experiments, the acceleration voltage

and current were set to 100 kV and 80 μA, respectively. Throughout a 360° rotation, 2368 projections are captured using incremental rotation steps. To enhance the signal-to-noise ratio, three radiographs are taken at each rotation angle and averaged. This rather low averaging level reduces the scan time and the risk of sample movement, which could blur the images. Each individual radiograph had an exposure time of one second.

The 3D images, representing the X-ray absorption field, are reconstructed from the recorded 2D radiographs using the *X-Act* software developed by RX Solutions. The voxel size is 8 μm, and the global dimensions of each 3D images are $2517 \times 2519 \times 1260$ voxels. With the chosen voxel size and our X-ray micro-tomography equipment, a full scan of the sample can be completed in two hours.

3 Image segmentation

As shown by the horizontal slice and the gray level profile depicted in Figures 2a & b, beads and the largest liquid bridges are distinguishable. However, the contrast between the small liquid bridges and the beads (see Figure 2c) is very poor because of the partial volume effect (PVE), which leads to mixed intensity values at the boundaries where different materials meet. As the voxel size is large relative to the volume of these small liquid bridges, PVE leads to their merging with connected beads or air. Moreover, the images exhibit some artefacts, such as ring artefact and a slight radial evolution of intensity (see Figures 3a & 5a), which also complicate the segmentation process.

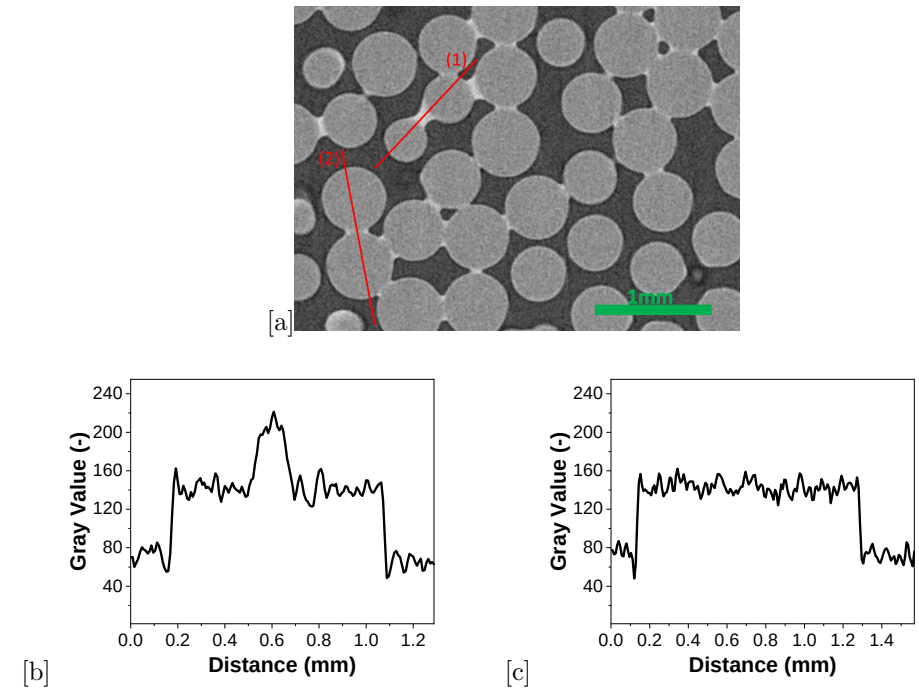

Fig. 2 a) A zoom in horizontal slice from the 3D image. The gray value profile for [b] a high contrast capillary bridge (line 1 in [a]), and [c] a low contrast capillary bridge (line 2 in [a]).

Segmentation using direct gray-level threshold to separate the different phases of the material is therefore not a viable approach, especially as the aim is to characterize liquid bridges. Instead, segmentation employing artificial intelligence (AI) offers a more promising solution, as existing algorithms can effectively distinguish phases with similar gray values [39–41]. These AI-based methods consider additional factors beyond gray values, such as shape, texture, and context of the different phases within the images.

In our segmentation methodology, we employ a two-tiered approach to optimize both accuracy and efficiency. Initially, we use the Random Forest algorithm [42], a traditional machine learning technique, as a preprocessing step. This approach leverages the Random Forest's ability to handle sparse labeling and provides preliminary classifications for image pixels. Then, we transition to a more specialized deep learning model, the U-Net neural network, for the primary segmentation task. The U-Net model, renowned for its effectiveness in biomedical image segmentation [43], refines and perfects the segmentation by building on the initial classifications generated by the Random Forest algorithm. This hierarchical approach ensures a robust and accurate segmentation by combining the strengths of both machine learning and deep learning techniques. In practice, all segmentation steps are performed using the Dragonfly software [44].

A recent study [45] adopts a similar approach for the precise segmentation of dehydrating gypsum. It employs a U-Net architecture alongside Random Forest classification to enhance the accuracy of phase segmentation within gypsum samples undergoing dehydration, which exhibits a more complex microstructure than the material studied here, both in terms of shapes and number of phases. This suggests that the segmentation workflow could be applied to other granular materials such as sands with irregular shape and other saturation conditions.

3.1 Preparation of Ground Truth Data

The success of AI models heavily relies on the availability of the right training data, as their effectiveness is rooted in learning from examples. In segmentation tasks, this learning process requires pairing raw images with their corresponding segmented masks. By internalizing the patterns, contrasts, and relationships present within these paired examples, AI models develop a robust understanding, enabling them to accurately segment new, unseen images. This essential input data is referred to as the ground truth.

Preparing the ground truth used to train and validate the U-net model is a pivotal step for image segmentation. We have adopted sparse labeling, a method in which only selected pixels, representative of different phases or classes in the image, are labeled, rather than exhaustively marking every pixel (Figure 3[a,b]). Traditional machine learning techniques like the Random Forest algorithm [42] are particularly well suited to the treatment of such sparse data. Based on the features of the labeled pixels - such as intensity, texture, and spatial coordinates - the Random Forest algorithm is trained to predict the labels of the remaining, unlabeled ones (Figure 3[c]). This streamlined approach thus accelerates the preparation of ground truth data by reducing the time required for manual annotation, but also efficiently leverages the power of the Random Forest method[45].

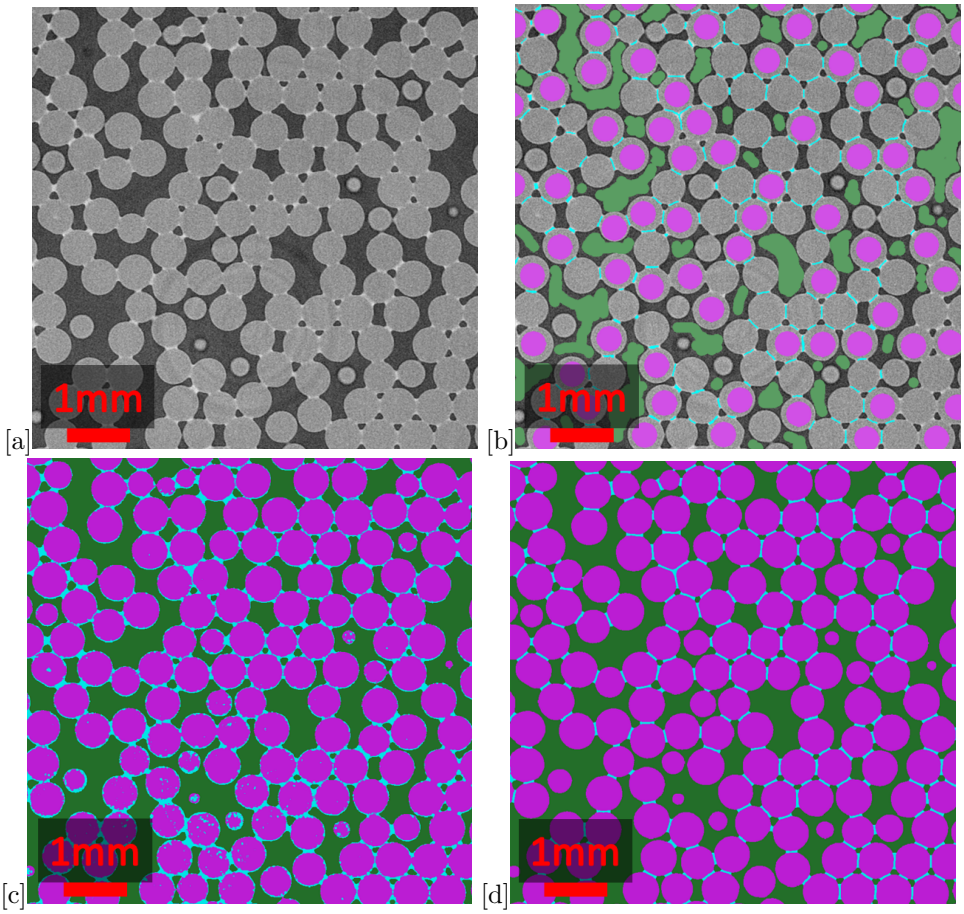

Fig. 3 a) Raw image, b) Manual assigning of pixels to each phase, c) Random forest first prediction with mislabeled pixels mainly at the perimeter and inside the beads surface d) The segmented mask after manual correction of sub-figure c. The air, polystyrene beads, and silicone oil are colored dark green, violet, and cyan respectively.

However, additional manual corrections are necessary (Figure 3[-d]). In particular, voxels at the border of the beads are incorrectly assigned to liquid because they appear slightly brighter over a thickness of 1-2 voxels (see Figure 2). This effect coincides with a localized decrease in gray values in the air adjacent to the beads, suggesting the presence of a phase-contrast artifact. Such artifacts are known to enhance edges [46]. This was confirmed by scanning a dry sample under similar acquisition conditions, resulting in the same artifact (see figure 4). However, it is also possible that a sub-voxel liquid film exists, which is expected in such samples. Scheel [47] estimated the thickness on a water/glass beads assembly to range between $10nm$ and $0.8\mu m$. If this were the case, the resolution would be insufficient to resolve the film thickness. Consequently, labelling these voxels as liquid could lead to a significant overestimation of the film volume due to the partial volume effect (PVE). Notably, observations at a

higher resolution ($2\mu m$ voxel size, see figure 17 in Section 4.4) did not reveal a clear liquid film either. Therefore, for all these reasons, the presence of these possible liquid films is neglected, and the voxels are reassigned to the beads. Other localized flaws, such as spurious liquid voxels within the beads, are also manually corrected.

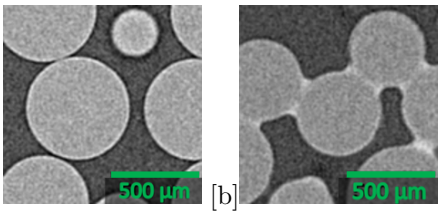

Fig. 4 A zoom of horizontal slice from the 3D image for a) dry, and b) wet sample.

Once corrections have been made, the manual selection of pixels from each phase is no longer necessary for subsequent images. Instead, only manual correction of mislabeled pixels after the Random Forest prediction is required. These two steps are repeated until a representative amount of data from the entire sample volume - the so called ground truth- is prepared (around six slices). This semi-automated process, which balances manual intervention with algorithmic learning, ensures a more accurate preparation of the ground truth while offering a time-efficient means of preparing the training data for the deep learning model. The time taken for preparing each segmentation mask was approximately 0.6-1 hour per slice. Note that preprocessing of the raw image was tested to facilitate ground truth generation, it was not adopted due to its lack of success (see Appendix and Section 3.2).

3.2 U-Net

After preparing the ground truth, our next step involves training a 2D U-Net network. The U-Net architecture is specifically designed for semantic segmentation tasks [39, 43, 45], making it particularly well-suited for our purpose. This network aims to identify and classify every pixel in the image, segmenting them into meaningful sections. To ensure the robustness and generalization capability of the model, 20% of the ground truth slices are excluded of the training and reserved for validation. This approach helps prevent the model from memorizing the training data and ensures its ability to effectively process and segment new, unseen images.

Training of the 2D-Unet model was based on a set of parameters which are described below. The *patch size* was set to 64 voxels, defining the dimensions of the subsections of the input images processed by the network at a time [48]. The *stride ratio*, set at 0.25, determines the overlap between these patches during the scanning process, enabling the model to consider bordering context and improve the continuity of the segmentation across patches. The model processed 128 patches simultaneously during training (batch size). Training was conducted over *100* epochs, with each epoch representing a full cycle through all batches of the training data. This number of epochs was found to be sufficient for the model to converge to a stable state, accurately learning to segment the images.

The loss function used was the Dice Loss, a variant of the Dice coefficient [49, 50]. The Dice coefficient measures the model's segmentation accuracy by comparing its predictions to the ground truth (see Appendix). It is particularly effective for unbalanced datasets, where one class is significantly less frequent than others. In our case, the liquid volume represents only 5% of the beads' volume. This choice helps ensure that the model does not become biased toward the more prevalent class. For the *optimization algorithm* [51], we employed Adadelta, an adaptive learning rate method designed to reduce the learning rate over time, enabling for finer adjustments to the model weights as training progresses. This approach helps prevent overshooting the minimum of the loss function, leading to more stable and accurate training [52].

Additionally, *data augmentation* was employed to artificially expand the dataset and enhance model's robustness. An augmentation factor of 10 was applied, meaning each image in the dataset was used to generate ten augmented variants. The augmentation techniques included *horizontal and vertical flipping*, *rotation* by 180 degrees, *zooming* in the range of 90% to 110%, and *shear* transformations of up to 2 degrees. These techniques simulate various imaging conditions and artifacts, ensuring the model can generalize across different scenarios and maintain accurate segmentation performance even under less-than-ideal conditions.

The computer time required for training the model is influenced by these parameters, including the number of images used for training and the computational capacity of the hardware. In this work, training the 2D U-Net model on 6 slides, each with dimensions of 2517 $\times$ 2519 pixels, took a total of 35 hours, with each epoch requiring approximately 21 minutes. This was performed using a 6GB NVIDIA GeForce GTX 1660 SUPER graphics processing unit (GPU), 128 GB random access memory (RAM), and Intel® Core^{TM} i7 - 10700 CPU @ 2.90GHZ.

The precision of the segmentation procedure was visually validated by carefully comparing the segmented slices directly to the original ones. An example of segmentation result, is presented in Figure 5. The model effectively segmented the volume into different classes, each corresponding to a specific phase: air, polystyrene beads, and silicone oil. The intrinsic quality of the original computed tomography images, including aspects such as noise levels, and any artifacts, plays a crucial role in the accuracy of segmentation [53]. However, these factors did not significantly affect the result of the segmentation, which was correctly carried out even in the presence of image artefacts. Moreover, as detailed in Appendix, the model showed good performance indicators with a final Dice coefficient of 0.984 ± 0.001 . Finally, the resulting volume fractions are $\phi_S = 0.60$ and $\phi_L = 0.029$, which are consistent with the experimentally added liquid content. In fact, in the compacted case, ϕ_S should be approximately equal to 0.60 for ϵ equal to 0.05 [13], resulting in ϕ_L being around 0.03. If we take a step further and estimate the contribution to the liquid fraction of the neglected liquid films surrounding the beads (considering the entire beads surface), given by $\phi_{L,f} = 6h\phi_S/d_p$, it ranges from 6×10^{-5} for a film thickness $h = 10nm$, to 5×10^{-3} for $h = 0.8\mu m$, leading to a maximum total liquid fraction of $\phi_L = 0.034$.

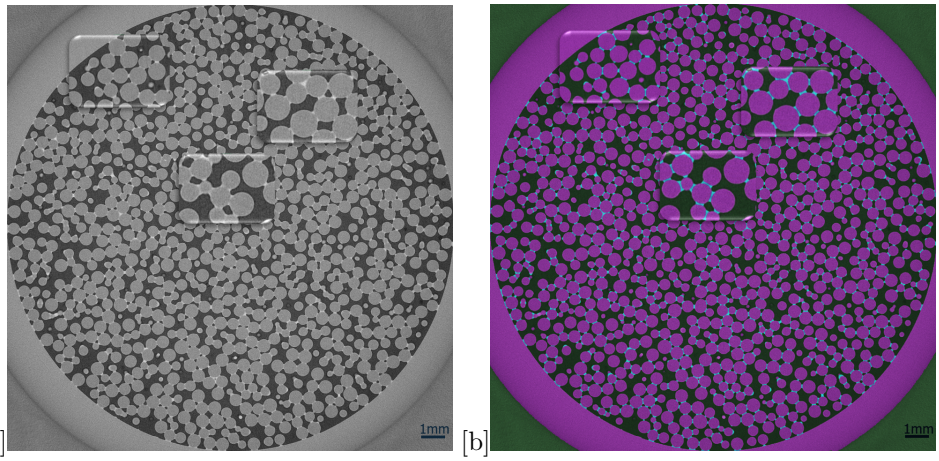

Fig. 5 Horizontal slice from the 3D image,8μm voxel size a) before segmentation b) after segmentation with the trained 2D U-net model. The air, polystyrene beads, and silicone oil are colored dark green, violet, and cyan respectively.

In an attempt to speed up and facilitate processing, the whole AI-based workflow has also been applied on pre-processed data, including phase contrast enhancement and denoising (see Appendix). However, this approach did not result in any significant improvement in the workflow's efficiency and lead to less accurate estimations of liquid and solid fractions. Consequently, direct processing of the raw data was chosen as the preferred method.

The trained model demonstrates robustness in effectively segmenting images with similar microstructure but varying voxel sizes, illustrating its adaptability across diverse imaging resolutions. However, it's important to acknowledge that while the model exhibits a certain degree of generalization, substantial deviations in microstructure may require retraining or fine-tuning to maintain accuracy.

4 Quantitative microstructure characterization

4.1 Local volume fraction

To further analyze the material's microstructure, we calculated the local fractions of liquid and grains within the sample by performing a 3D convolution operation with a uniform kernel (mean filtering) on binary images of liquid or grain phases. This approach effectively averages the presence of liquid or the grain phase over local volumes. The size of the kernel (the side of the cube), or window size (ws), determines the scale of local averaging, offering for flexible examination of the microstructure at various scales of interest.

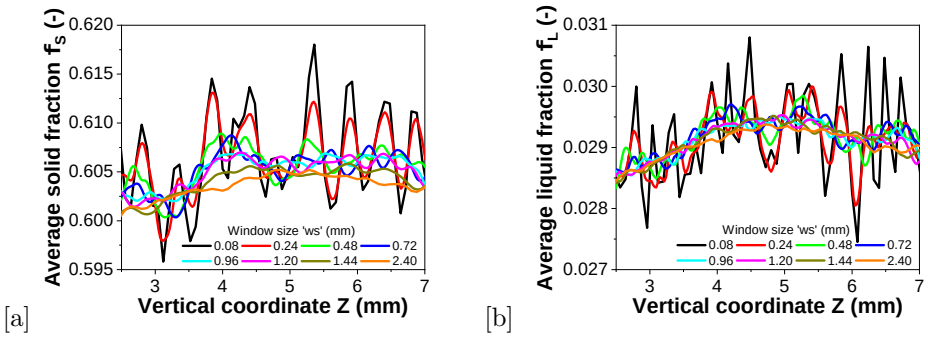

[a] [b]

Fig. 6 Semi-local solid and liquid fractions of reference sample (without shear) evaluated from averaging the local volume fractions obtained by 3D convolution with different window sizes.

To quantitatively characterize spatial distributions of liquid and solid at a larger scale, semi-local volume fractions are computed by averaging the local volume fractions on subvolumes of the images. In Figure 6, vertical profiles are generated by averaging the local fractions obtained from the convolution calculations over each horizontal slice of the image (i.e at each height Z). This figure shows the evolution of the resulting liquid and solid semi-local fractions for several window sizes, as a function of the sample height. As expected with such measurements (see e.g. [54]), porosity fraction fluctuations increase with decreasing window size. For further analysis, a relatively small window size of $ws = 0.96mm$ (i.e. side of the cube, $ws \approx 1.75 \times d_p$) was selected to capture local trends while minimizing large fluctuations and ensuring computational efficiency. This approach allows for the observation of the spatial distribution of liquid within the sample and its evolution under shear, as shown in Figure 7, where the liquid is seen to cluster by shearing.

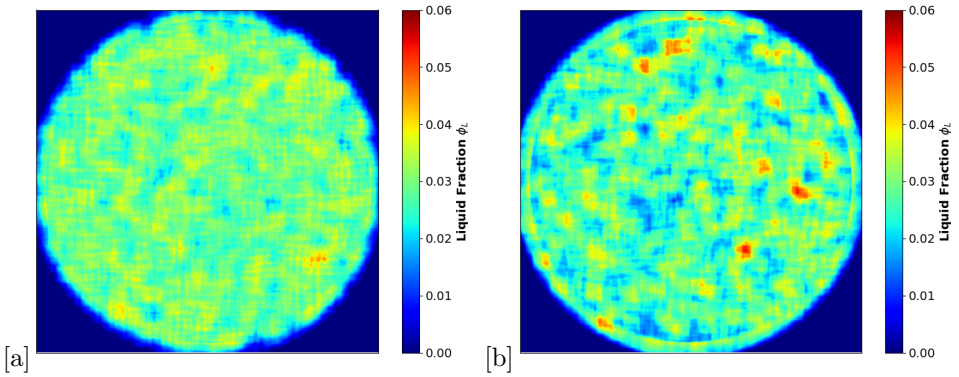

[a] [b]

Fig. 7 Maps of the local liquid volume fraction ϕ_L at the middle height (H/2) of the a) reference sample, and b) after 10 minutes of shear.

The distributions of solid fraction ϕ_S and liquid content $\epsilon = \phi_L/\phi_S$ across the sample's height, are depicted in Figure 8. Initially, Φ_S and ϵ are quite homogeneous

along the height. However, as deformation progresses, the solid volume fraction Φ_S consistently decreases, particularly near the upper regions of the sample. This decrease in Φ_S with increasing deformation suggests that the sample become less densely packed due to the rearrangement and dilation induced by shear forces. The more pronounced decrease in Φ_S near the top indicates that these regions are more significantly affected by the deformation, likely due to shear localization. The observed shear localization and volume changes are consistent with previous findings [55–58], where digital image correlation (DIC) on 3D X-ray CT volumes provided full-field displacement and strain measurements.

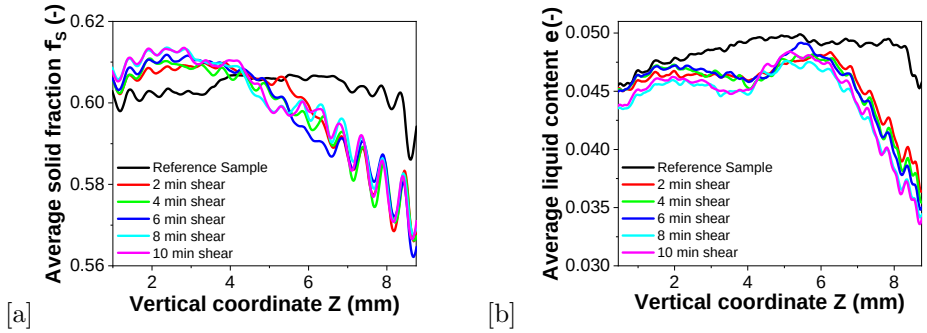

Fig. 8 Vertical profile of (a) solid fraction ϕ_S and (b) liquid fraction $\epsilon = \phi_L/\phi_S$ at different times.

Figure 9 illustrates the variations of the solid and liquid fractions in the radial direction, segmented into the bottom, middle, and top regions of the sample under shear deformation. The semi-local volume fractions are computed using concentric layers with a thickness of 0.96 mm in the radial direction (R). In the vertical direction (Z), larger intervals were used to correspond to the three regions identified in figure 8a—bottom, middle, and top—based on their distinct solid fraction profiles along the sample height. This allows for a detailed analysis of the radial distribution of Φ_S and Φ_L within these regions, illustrating the effects of shear deformation in the sample. Figures 9a, c, and e demonstrate that in the bottom part of the sample ($Z < 3.84mm$), there is a slight compaction, indicating by a small increase in ϕ_S. This compaction contrasts with the dilation observed in the top part of the sample ($Z > 5.76mm$), where ϕ_S decreases. Between the regions, a transition zone occurs for $3.84 < Z < 5.76mm$, where the sample exhibits intermediate behavior between compaction and dilation.

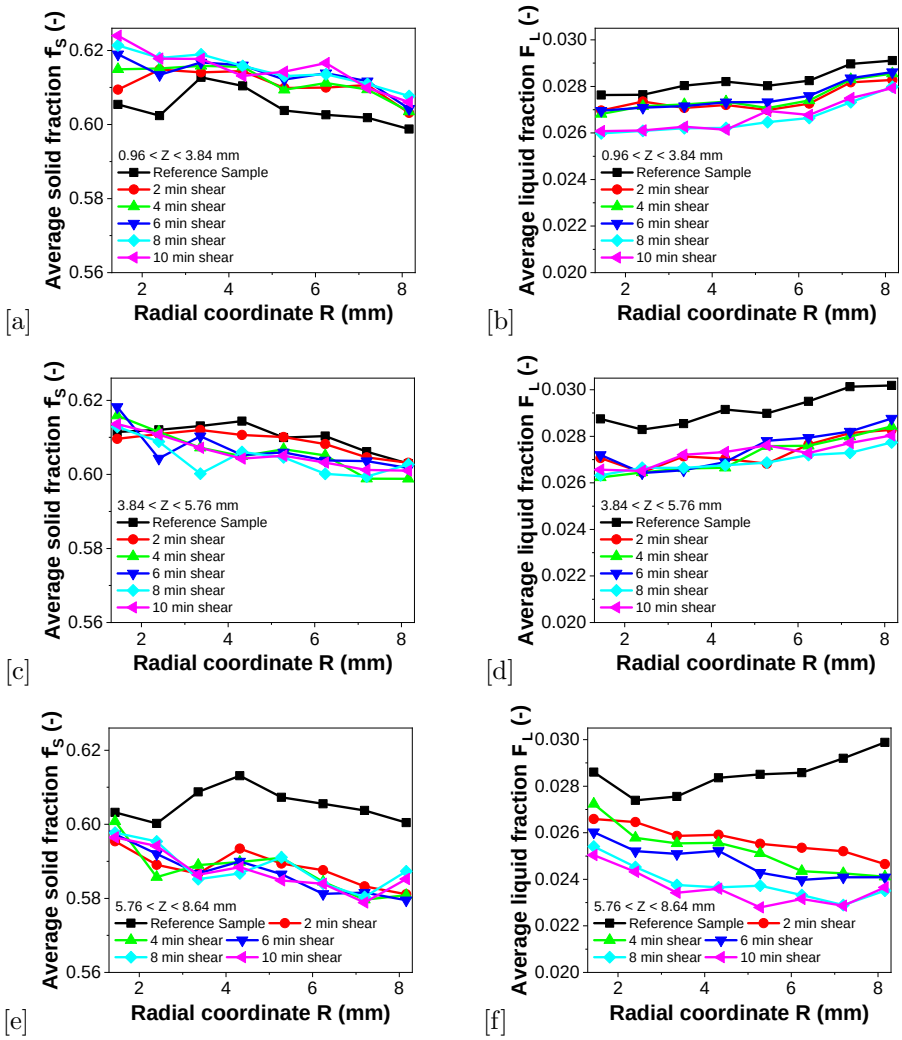

Fig. 9 Radial profiles of (a, c, e): solid fraction ϕ_S and (b, d, f) liquid fraction ϕ_L and evolution with shear time in bottom, middle and top parts of sample, respectively.

These findings suggest that although the shear deformation predominantly affects the upper portion of the sample—leading to significant dilation—the lower portion also experiences deformation, resulting in slight particle rearrangement and compaction. So, the sample undergoes a net dilation due to shear forces, with more pronounced effects in the upper regions. This behavior highlights the non-uniform nature of deformation within the sample, emphasizing the localized impacts of shear forces depending on the height within the sample.

During the shearing process, a noticeable decrease in liquid content ϵ is observed over time as shown in Figure 8b. This trend is consistent with findings from numerical

studies that suggest significant reductions in liquid volume within shear zones [33]. This decrease is primarily attributed to the expulsion of liquid from regions that are highly deformed by shear forces, leading to a net loss of liquid within the sample.

Quantitatively, the liquid content in the sample decreases from an initial value of $\epsilon = 0.048$ in the reference state to $\epsilon = 0.044$ after 10 minutes of shear (the amount of liquid present in the sample decreases for growing shear strain, and the lost amount is found outside the sample container at the bottom of the geometry, in the zone highlighted by white rectangles in Figure 1b). This decline is further illustrated in Figures 9b, d, and f, which show the liquid fraction's reduction with increasing deformation across different parts of the sample. These figures reveal that the liquid fraction decreases not only near the top, where shear-induced deformation is most intense, but also across the entire sample, albeit to varying degrees depending on the region. The expulsion of liquid, particularly from the top, more deformed sections, underscores the influence of shear forces on liquid redistribution within granular materials. The decrease in ϵ suggests that as the sample is sheared, the liquid migrates out of the most deformed zones, contributing to the overall reduction in liquid content observed throughout the sample. This behavior has important implications for understanding the rheological properties of wet granular materials under shear.

4.2 Automatic classification of liquid morphologies

Figure 10 shows several typical liquid morphologies extracted from the segmented images , illustrating the diverse forms that liquid structures can take within the granular material. One of the key objectives of this study is to distinguish between these morphologies and to track how they evolve under shear strain.

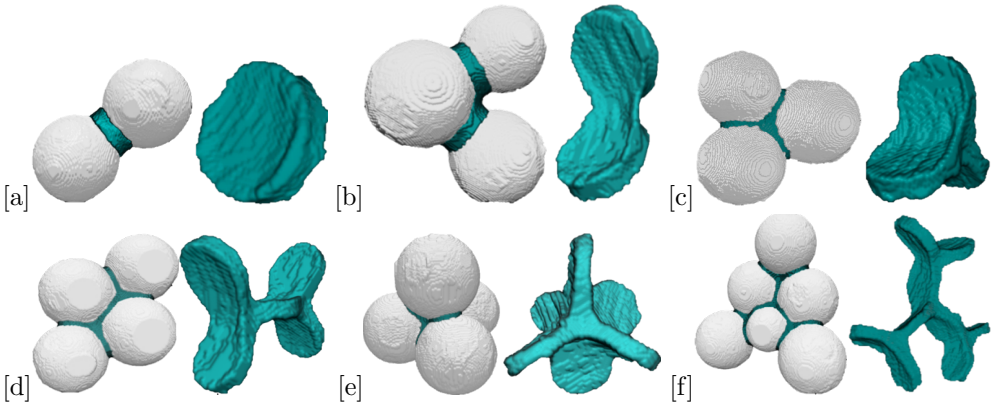

Fig. 10 Extracted liquid morphologies from the sample after segmentation, which has been visually and quantitatively validated as explained in section 3.2 and Appendix (3D rendering of stacked segmented slices, Dragonfly software [44]). a) Liquid or capillary bridge (cb): two neighboring grains in contact, b) Dimer (di), and c) Trimer (tr): three neighboring grains in contact, d) Pentamer (pt), and e) Tetrahedral (th): four neighboring grains in contact, and f) others: big liquid morphology with five or more neighboring grains in contact.

Due to the high number of liquid morphologies present within a single sample, manual classification would be impractical and inefficient. Therefore, an automatic classification procedure was developed to systematically categorize the liquid morphologies.

Figure 11 presents the relationship between the volume and surface area for each connected component within the liquid phase, as identified from the segmented images. In contrast to the findings of Scheel et al. [15], where distinct clusters corresponding to specific liquid morphologies were evident, our analysis did not reveal any clear clustering patterns that could be associated with particular morphologies. The clustering results of liquid morphologies presented in this study show differences compared to those reported by Scheel et al. [15]. While both studies examine similar systems, key differences in granular material properties (e.g., bead size and type, liquid characteristics), imaging resolution, and segmentation methodologies may contribute to these discrepancies. Despite these efforts to identify potential factors, the exact source of the divergence remains unexplained. However, these variations highlight the importance of experimental and methodological details in studies of liquid morphologies. Further investigations would be required to fully understand the observed differences.

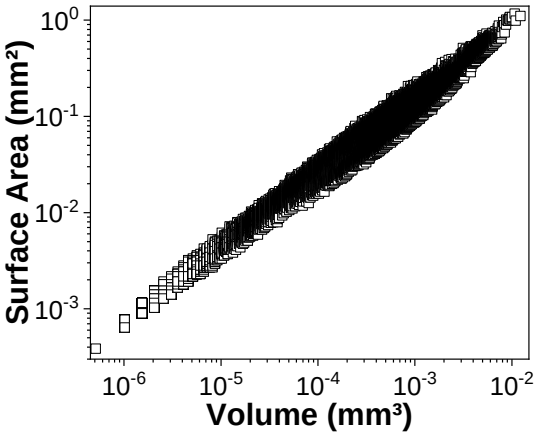

Fig. 11 The liquid surface area versus the volume of all liquid morphologies as obtained by X-ray micro-tomography.

To do so, a watershed transform was performed on the solid phase, allowing for the separate identification of each grain. This technique effectively segments the granular material, isolating individual grains and facilitating the subsequent analysis. Following the identification of grains, both the grains and liquid regions were labeled to allow for a detailed examination of their interactions.

Subsequently, inside bounding boxes defined around each liquid region, the liquid volume was dilated. This dilation simulates the expansion of the liquid into adjacent areas, helping to identify distinct grain labels that share boundaries with the liquid

morphology. The entire image processing workflow, including the watershed transform, grain labeling, and dilation of liquid volumes, was implemented using the scikit-image Python library [59]. This approach ensures a robust and reproducible method for analyzing complex liquid morphologies in granular materials.

Table 1 Geometrical descriptors calculated for each liquid morphology

Geometrical descriptor	**Unit**
Volume	μm^3
Surface area	μm^2
Volume/Surface area	μm
Minimum Feret diameter	μm
Mean Feret diameter	μm
Maximum Feret diameter	μm
Minimum ortho Feret diameter	μm
Minimum ortho/Maximum Feret diameter	-
Minimum ortho/Minimum Feret diameter	-
Minimum ortho/Mean Feret diameter	-
Max Feret/Mean Feret diameter	-
3D solidity	-
Sphericity	-
Aspect ratio	-

Several specimens representing each morphology were manually identified and characterized using the geometric descriptors summarized in Table 1, as well as the number of contact grains. To quantify the 3D solidity of the specimens, the ratio of the surface area to the convex hull surface area was calculated, following the method outlined by [60, 61]. A solidity value of 1 corresponds to a perfectly smooth and solid object, while values less than or greater than 1 indicate an irregular boundary or the presence of holes.

The definition of sphericity used aligns with the concept introduced by Wadell [62], which quantifies the extent to which a particle's shape approximates a perfect sphere. The sphericity is calculated using the formula, implemented in the Dragonfly software [44]:

$$\text{Sphericity} = \frac{\left(6 \cdot \pi^{\frac{1}{2}} \cdot V_p\right)^{\frac{2}{3}}}{A_p}, \tag{1}$$

where V_p is the particle's volume, and A_p is the surface area. The surface area is determined using the Lindblad surface area estimator [61], a reliable computational method for estimating surface area from digitized 3D objects.

These characteristics were examined to explore potential relationships between various pairs of variables. Despite extensive analysis, no significant correlation were observed among most of the variables.

However, a noteworthy exception was found when comparing the aspect ratio – calculated as the ratio between the smallest and largest eigenvalues of the inertia

tensor – against the number of grains in contact for each liquid . This specific relationship led to the establishment of a separation criterion for automatic classification, as demonstrated in Figure 12 and detailed in Table 2.

This correlation is particularly significant because the aspect ratio and the number of contact grains serve as dimensionless metrics. As a result, they provide a robust and generalizable method for classifying liquid morphologies that is independent of the voxel size of the scans used. This finding not only facilitates the automatic classification of liquid morphologies but also ensures that the methodology can be applied across different resolutions without loss of accuracy.

Table 2 Criteria on aspect ratio and contact grains number to identify each liquid morphology type

Morphology type	Contact grains number	Aspect ratio
Edge capillary bridge (ecb)	1	[0.3-0.6]
Capillary bridge (cb)	2	[0.4-0.75]
Dimer (di)	3	[0.1-0.3]
Trimer (tr)	3	[0.4-0.75]
Pentamer (pt)	4	[0.2-0.5]
Tetrahedral (th)	4	[0.55-0.95]
others	5	[0.1-0.6]

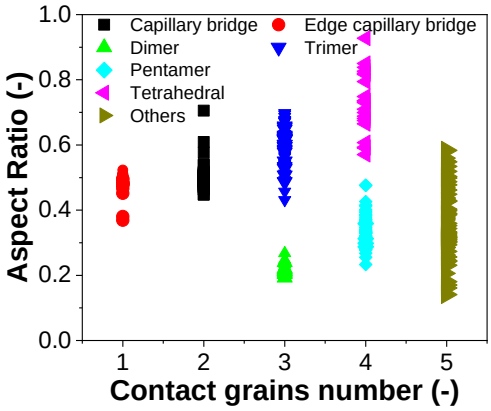

Fig. 12 The aspect ratio versus the number of contact of each liquid morphologies. Edge capillary bridges is the capillary bridges formed between one grain and the edge of the sample container.

The classification results for liquid morphologies in the sample after 10 minutes of shear have been captured in a supplementary video, which provides a visual representation of the morphologies' distribution and evolution. This classification enables a more detailed analysis of the liquid distribution across different types of morphologies.

Figure 13a presents the proportion of the total liquid volume occupied by each morphology type. Notably, capillary bridges dominate the liquid volume across all shear steps, although their share decreases from approximately 85% to 70% as shear progresses. This suggests that while capillary bridges are initially the most prevalent morphophy, shear deformation induces a redistribution of the liquid, leading to a reduction in their overall volume.

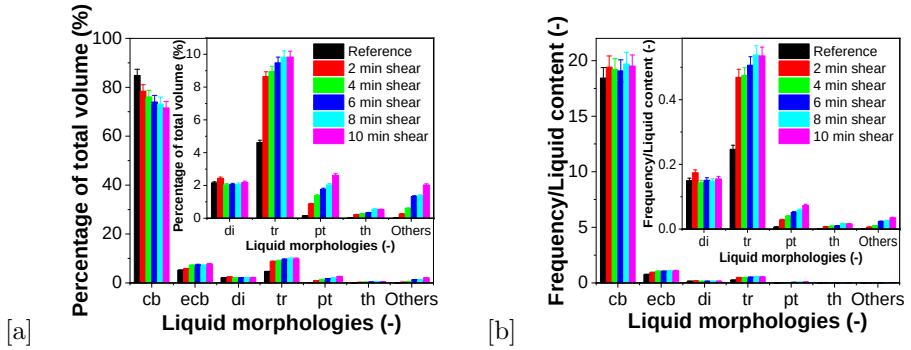

Fig. 13 a) The percentage of the total liquid volume occupied by each liquid morphologies (sum of the volumes of all liquid bridges on each morphology category), and evolution with shear deformation. The error bars represents the percentage of volume of unclassified liquid morphologies. Inset: zoom-in to focus on large morphologies, and b) Ratios of each morphology number with respect to the total number of morphologies and their variation with shear deformation. The error bars represents the frequency of unclassified liquid morphologies. Inset: zoom-in to focus on large morphologies.

Furthermore, Figure 13b shows the normalized frequency of each liquid morphology, calculated as the ratio of the number of each kind of morphology over the total number of morphologies. This frequency is normalized by the liquid content for each step to account for the observed liquid loss during shearing (as detailed in Figures 8b and 9f). The analysis reveals a slight increase in the frequency of capillary bridges with continued shearing, suggesting that these morphologies become more prominent under deformation.

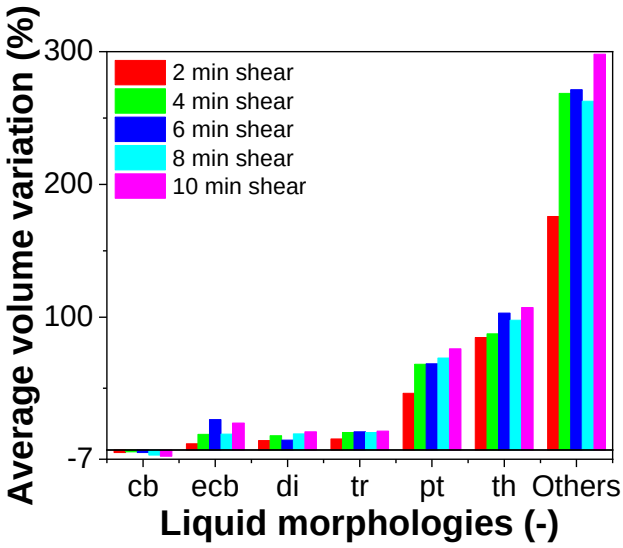

Fig. 14 The variation of average volume of each liquid morphologies with shear deformation.

In addition, Figure 14 displays the variation of average volume of various liquid morphologies with respect to the reference sample. While the average volume of capillary bridges remains relatively stable, the average volume of larger liquid morphologies increases with deformation. This trend suggests that under shear stress, liquid tends to coalesce into larger clusters, consistent with the observations of liquid volume fraction maps shown in Figure 7.

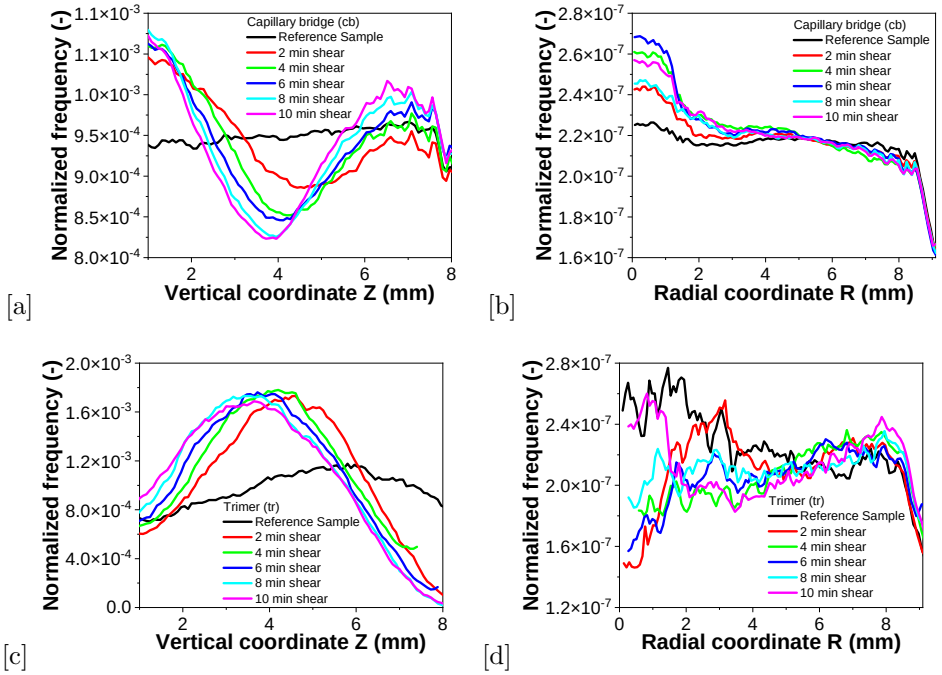

Fig. 15 Vertical and radial profiles of capillary bridge and trimer densities, for different shear strains.

Moreover, the spatial distribution of liquid morphologies under shear deformation is further analyzed in Figure 15. This figure tracks the position of liquid morphologies within the sample and highlights several key trends. For instance, the frequency of capillary bridges increases at both the top and the bottom of the sample while it decreases in the middle regions (Figure 15a). Capillary bridges become more concentrated near the central axis of the sample (Figure 15b). Conversely, the frequency of the trimers decreases at the top of the sample and increases in the other areas (Figure 15c). Radially, there is a decrease in the frequency of trimers near the central and an increase near the edges of the sample (Figure 15d), correlating with the observed increase in local liquid fraction at the edges, as shown in Figure 7.

4.3 Coordination number

4.3.1 Radial distribution function

Figure 16 presents the Radial Distribution Function (RDF), also known as the pair correlation function, calculated from the positions of the bead centres identified in the labelled images, using the *rdfpy* python module [63]. The RDF, quantifying the density of grain centres at distance r from the centre of a reference grain, is a classical microstructural descriptor of particle packings [64, 65]. The graph of RDF $g(r)$, as previously observed in microtomography experiments on spherical ball packings [66] and in numerical simulations [67], exhibits a very large peak at distance r equal to

average diameter d_p, corresponding to neighboring grains at contact, or nearly in contact. Due to the polydispersity of our particles, the Dirac mass associated with contacts in a packing of strictly monosized beads spreads over an interval of order 5×10^{-2} in units of d_p. Moreover it should be recalled that the contacting neighbors are difficult to distinguish from close neighbors without contact, since the RDF, at least in the dry cohesionless systems studied in Refs. [66, 67], tends to diverge as r approaches d_p.

The secondary peaks at $r/d_p = \sqrt{3}$ and $r/d_p = 2$, followed by a fast drop, are also similar to the observations of the previous observations of Ref. [66], although less sharp than in the simulations of ideally monodisperse systems of Ref. [67].

Function $g(r)$, by construction, expresses directionally averaged correlations. In the present study of sheared bead assemblies, the angular dependence of pair correlations should exhibit the corresponding anisotropy, and differ from the isotropic microstructure of Ref. [67, 68], and from the presumably orthotropic ones of Ref. [66]. Angular distributions of close, interacting neighbor grains in sheared systems are characterized in the numerical simulations of Ref. [36].

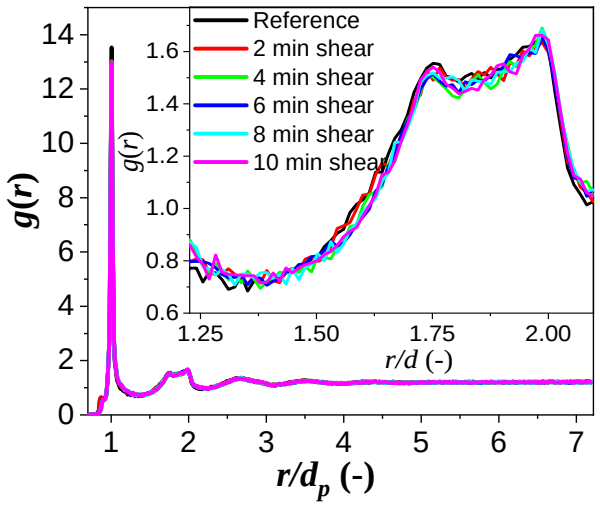

Fig. 16 Radial distribution function $g(r)$ versus distance r in sheared bead packing. Inset: blown-up detail of second and third peaks.

4.3.2 Estimation of Z_c

The coordination number Z, or average number of interactions per particle, may be written [36] as $Z = Z_C + Z_D$, the sum of the contact coordination number Z_C, and the distant coordination number Z_D, counting the average number of neighbours interacting by a liquid bridge without contact.

Using the RDF, the contact coordination number Z_C can be roughly estimated as follows:

$$Z_C = 4\pi\rho \int_{r_i}^{r_o} g(r) r^2 \, dr, \tag{2}$$

where ρ denotes the number density of the grains using bounds r_i and r_g close to d_p. Using $r_i = 0.95 d_p$ and $r_o = 1.05 d_p$, Z_C is estimated at 5.5. This coincides well with values reported in numerical simulations of systems with the same rheological properties [36]. This agreement contrasts with the difficulty of measuring the coordination number in the experiments of dry bead packings of Ref. [66], in which estimates exceeding the maximum value of 6 (see, e.g., [67] and references therein for a justification of this upper bound) are reported. This could be due to different statistics of small intergranular distances in wet assemblies, despite the similar shape of RDFs. The accuracy of Z_c, as estimated with Eq. 2, and its sensitivity to the choice of bounds r_i and r_o, should be tested in numerical simulations.

4.3.3 Estimation of Z_D

In the pendular regime, capillary bridges (cb) are the most common form of liquid morphology, significantly outnumbering other liquid clusters such as trimer (tr), pentamers (pt), tetrahedral (th) , and others. To estimate the distant coordination number Z_D, we normalize the number of capillary bridges (excluding those at the sample's edge) by the number of grains N_g, and subtract the estimated contact coordination number Z_C.

For the reference sample, Z_D is approximately 3.2, which is consistent with the results from numerical simulations [36]. As the sample undergoes shearing, Z_D decreases to around 2.75. This decrease in Z_D can be attributed to the dilation of the sample under shear, which increases the average distance between grains and reduces the number of capillary bridges formed between them.

4.4 Effect of voxel size

To explore the impact of voxel size on the segmentation and analysis of the material's microstructure, an additional scan was conducted on the same material with a liquid fraction of $\epsilon = 0.015$ using a finer resolution of $2\mu m$ per voxel. This high-resolution scan was performed using the same X-ray imaging setup as previously described.

The 3D images were acquired using a Varex 4343 DX-I imager (for each projection: 3032 x 3032 pixels, pixel pitch is 139 microns) and the X-ray source Hamamatsu L10711-23 (maximum voltage: 160kV). The scan was conducted with an acceleration voltage of $100kV$ and a current of $40\mu A$. During the scan, the sample was rotated through 360°, and 2368 projections were acquired at incremental rotation steps. To enhance the signal-to-noise ratio, ten radiographs were taken and averaged at each rotation angle, with each radiograph having an exposure time of one second.

The acquired 2D radiographs were then used to reconstruct 3D images of the material, capturing the X-ray absorption field. This reconstruction was performed using the X-Act software developed by RX Solutions, the same software used for the initial scans. The overall dimensions of the reconstructed 3D images were $2919 \times 2919 \times$

1309 voxels. However, due to image artefacts at the periphery, only the central region, with dimensions $688 \times 688 \times 688$ voxels was selected for further analysis as shown in Figure 17a.

To directly compare the high-resolution data with the initial scans, the high-resolution images were downscaled to match the initial voxel size of $8\mu m$. This was achieved by averaging groups of 4x4 adjacent voxels (binning process), resulting in new image dimensions of $172 \times 172 \times 172$ voxels (Figure 17b). With the chosen voxel size (i.e $2\mu m$) and our X-ray micro-tomography equipment, a full scan of the sample was performed in about six hours. We employed the analytical procedures previously described to segment and evaluate both data sets.

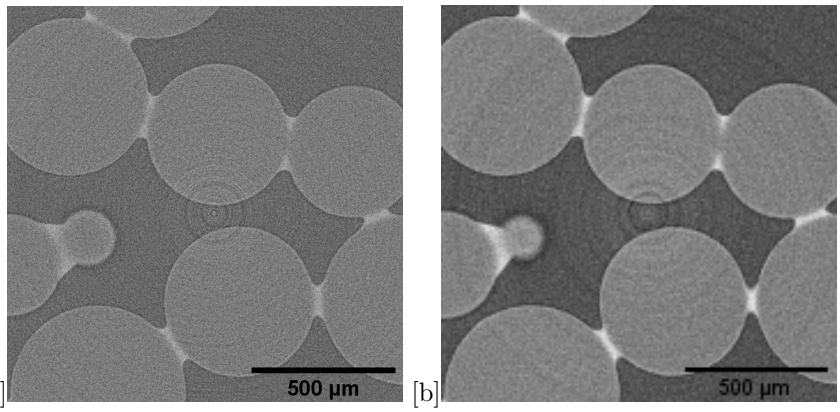

Fig. 17 Horizontal slice from the 3D image before and after downsampling: a) $2\mu m$ voxel size, and b) $8\mu m$ voxel size.

The data presented in Figure 18 highlight the impact of voxel size on the average solid fraction (ϕ_S) and liquid fraction (ϕ_L) across the sample height, comparing results obtained using voxel sizes of $2\mu m$ and $8\mu m$. These fractions calculated using a convolution filter with a window size of $ws = 0.24mm$).

The results suggest that using a larger voxel size, such as $8\mu m$, may result in a slight underestimation of the solid fraction ϕ_S compared to the finer $2\mu m$ resolution. This discrepancy can be attributed to the partial volume effect, where larger voxels may not fully capture the fine details of the granular boundaries. Consequently, voxels near the solid-liquid interface may be misclassified, particularly in cases where the voxel contains both solid and liquid components. The finite voxel size creates an averaging effect, smoothing out the precise boundaries and transitions between phases.

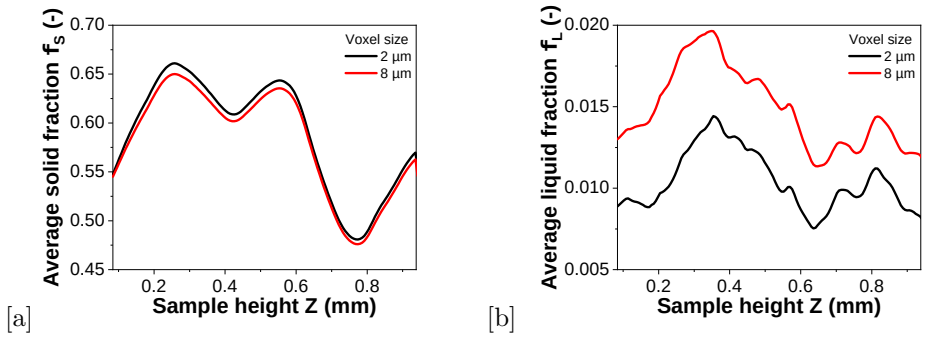

Fig. 18 Effect of voxel size on a) the solid fraction ϕ_S and, b) the liquid fraction ϕ_L.

Regarding the liquid fraction, the use of a larger voxel size ($8\mu m$) leads to overestimate the volume of liquid bridges between the grains, with a range between 21% and 42%. This directly affects the quantification of the liquid fraction. After accounting for this overestimation in the reference sample, the liquid fraction ϕ_L was revised to 0.022 from the originally estimated 0.029. This correction underscores the need for caution when interpreting absolute volume measurements obtained from X-ray microtomography, especially for small features where voxel size is large relative to the object size.

Importantly, while the absolute volume of capillary bridges is affected, the variations in volume fraction across the sample and with deformation remain unaffected by voxel size changes. This suggests that while the accuracy of absolute values is resolution-dependent, trends and relative changes in liquid distribution can still be reliably captured. Furthermore, the number of capillary bridges detected in the reference sample remains consistent at 38 bridges across both voxel sizes, indicating that the number of liquid morphologies is not influenced by resolution changes, only their measured volumes.

The visual comparison of the extracted liquid bridges at different resolutions further complements the quantitative data (Figure 19). The bridges obtained from the downscaled (binned) image (Figure 19b) exhibits strong similarity to those derived from the images directly acquired at an $8\mu m$ voxel size (Figure 10a). While the global shapes of the bridges remain consistent across both resolutions, the finer details are more evident in the high resolution images. The main difference appears in the thickness of the liquid bridge at its center. The high-resolution suggest the possibility of direct contact between grains, as the bridges seem thinner in this central region. However, this observation does not conclusively prove that grain-to-grain contact occurs, as the liquid film in these regions could be thinner than the voxel size. During segmentation, such thin liquid films may have been classified as part of the grains, merging with the beads and obscuring the precise nature of the contact.

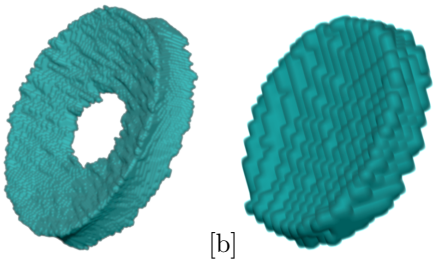

[a] [b]

Fig. 19 Effect of voxel size on the shape of liquid bridge a) $2\mu m$, b) $8\mu m$ (binning).

These observations underscore the limitations related to the finite resolution of the images in the analysis of multi-phase materials. They serve as a crucial reminder that while computational tools and deep learning models offer powerful means for image analysis and segmentation, the fidelity of the input data, as governed by voxel size, remains a fundamental factor. It directly affects the accuracy and reliability of the results, emphasizing the importance of careful consideration and optimization of voxel size in such analyses.

5 Conclusions

This study presents a comprehensive investigation into the segmentation, classification, and morphological analysis of liquid structures within wet granular materials under shear, using advanced deep learning techniques and 3D X-ray microtomography. The primary objective was to characterize the evolution of liquid morphologies, particularly capillary bridges, in response to shear deformation.

Key findings of this research include:

1. **Segmentation Accuracy and Robustness:** The segmentation approach, combining Random Forest and U-Net models, demonstrated high accuracy and adaptability. The methodology effectively segmented the material into distinct phases (air, polystyrene beads, and silicone oil) despite low contrast and image artifacts. This robustness highlights its potential for generalizing across different imaging conditions and microstructures.
2. **Liquid Morphology Classification and Distribution:** The study developed an automated classification procedure to categorize various liquid morphologies. By quantifying geometric descriptors and grain contacts, it was observed that capillary bridges dominate the liquid distribution. Their volume fraction decreases under shear, while their frequency increases, reflecting redistribution. Larger liquid morphologies tend to cluster and grow with shear, consistent with liquid redistribution and clustering behaviors in the material.
3. **Microstructure Evolution under Shear:** Shear deformation leads to significant changes in the spatial distribution of solid and liquid phases. Solid fraction decreases in shear-localized regions, while liquid content diminishes as liquid is expelled from highly deformed zones. Coordination number analysis indicates that shear induces local rearrangements without drastically altering the overall packing structure in the quasi-static regime.

4. **Validation and Future Directions:** The methodology was validated by reproducing known behaviors, such as the decrease in liquid bridges and redistribution of liquid in dilative shear zones. Resolution analysis showed that voxel size influences volume quantification, with larger voxels overestimating capillary bridge volumes. While higher-resolution data provided finer morphological details, challenges remain in accurately capturing thin liquid films and complex grain-liquid interactions. Future work should explore higher-resolution imaging or alternative techniques to resolve ambiguities and extend the methodology to more complex systems, including varying liquid content and viscosity effects.

This study provides a robust framework for analyzing the microstructure and rheology of unsaturated wet granular materials, bridging experimental observations and theoretical models. By advancing segmentation and classification techniques, it paves the way for investigating complex behaviors in granular materials and their applications in geotechnics, material science, and beyond.

Appendix . In an attempt to improve the initial image preparation process, three types of input image were used, each leading to distinct ground truth and consequently different segmentation models (referred to as Process A, B, and C respectively). The first type is the reconstructed raw image without any correction or filtering (Process A, Figure 20a). The second type was enhanced with phase contrast correction (Process B, Figure 20b). X-rays undergo phase shifts when passing through various materials, altering their intensity. Phase contrast correction methods estimate these shifts to improve image contrast, a process executed at the image reconstruction stage using the X-Act software by RX Solutions. The third input image was obtained by denoising the phase contrast images, utilizing a total variation filter as described in [69] (Process C, Figure 20c).

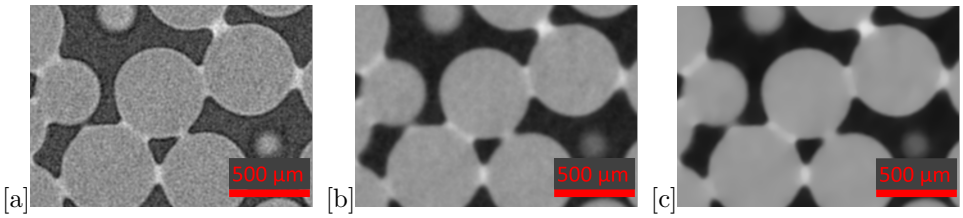

Fig. 20 Example of the input images for the three processes A, B, and C: a) Raw image, b) with Phase contrast enhancement, and c) with denoising filter.

Figure 21 shows the solid volume fraction ϕ_S and the liquid volume fraction ϕ_L obtained from the segmented images using the three trained models. It is observed that the model trained on the raw images without phase contrast nor denoising (Process A) provides the volume fractions that best matches the experimentally added liquid content. In fact, in the compacted case, ϕ_S should be approximately equal to 0.60 for ϵ equal to 0.05 [13], resulting in ϕ_L being around 0.03.

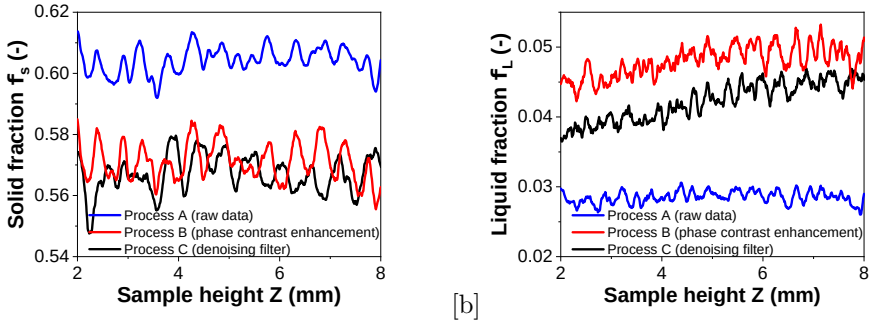

[a] [b]

Fig. 21 a) The solid volume fraction ϕ_S, b) the liquid volume fraction ϕ_L obtained from the three processes A, B, and C.

Processes B and C exhibit lower precision due to the challenge of correctly assigning voxels at interfaces between phases. This miss-assignment occurs in both smoothed images and images with phase contrast correction because these operations tend to smooth images and spread interfaces. Consequently, processes B and C underestimate ϕ_S and overestimate ϕ_L.

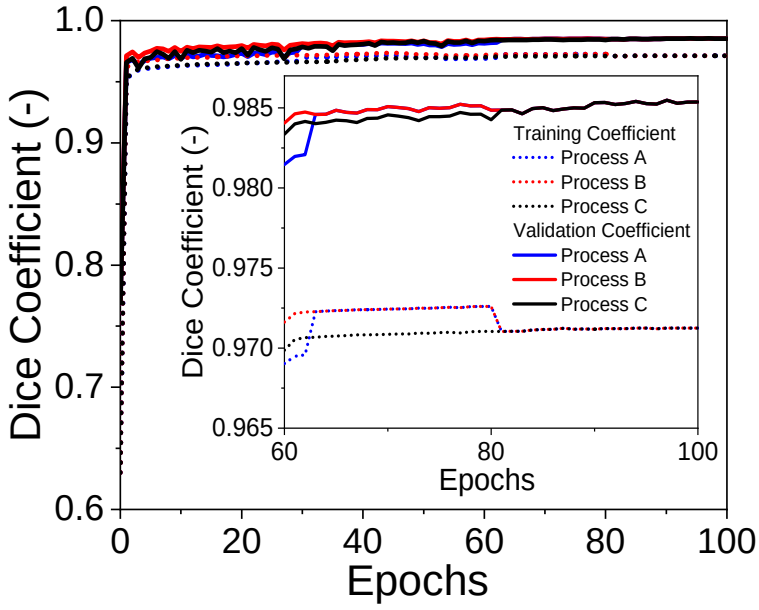

[a]

Fig. 22 Training and validation Dice coefficient for the three processes A, B, and C

Figure 22 displays the Dice coefficient for both the training and validation datasets as the models trained over multiple epochs. The Dice coefficient [49, 50] measures how well the model segments images by comparing its predictions to the ground truth. It is calculated using the below formula:

$$\text{Dice Coefficient} = \frac{2 \times |U \cap V|}{|U| + |V|} \tag{3}$$

where U is the set of pixels predicted as positive, and V is the set of pixels that are actually positive according to the ground truth. The numerator $2 \times |U \cap V|$ represents twice the number of correctly predicted positive pixels, known as true positives, while the denominator $|U| + |V|$ is the sum of all predicted positive pixels and all actual positive pixels. This formulation allows the Dice coefficient to effectively quantify the overlap between the predicted and ground truth segmentation's, ranging from 0 (no overlap) to 1 (perfect overlap).

Throughout the training process, both the training and validation Dice coefficients for all three models rise towards a high value of approximately 0.984 ± 10^{-3}. This high Dice coefficient indicates that the models predictions closely match the ground truth data. The small difference between the training and validation Dice coefficients suggests that the models are equally precise in segmenting both the training data and the unseen validation data, further confirming their robust performance. It's worth noting that process C converges faster as shown by the inset of Figure 22 (it needs around 65 epochs) but wasn't chosen because it overestimates the volume of liquid morphologies due to the reasons explained before.

Acknowledgements. We are grateful to David Hautemayou and Cédric Mézière for technical help with the measurements. Funding from Agence Nationale de la Recherche within the frame of the national program Investments for the Future ANR-11-LABX-022-01 and project "RheoGranoSat" - ANR-16-CE08-0005-01, is gratefully acknowledged.

Author contributions. AA and PA carried out the x-ray experiments, implementing concepts supplied by AF & CC; data analysis by AA; data interpretation done by JNR, AF, CC & AA; AA wrote the original draft of the paper, which was thoroughly reviewed by PA, JNR, AF & CC.

Declarations. The authors declare no competing interest.

References

[1] Mitarai, N., Nori, F.: Wet granular materials. Advances in Physics **55**(1-2), 1–45 (2006)

[2] Iveson, S.M., Litster, J.D., Hapgood, K., Ennis, B.J.: Nucleation, growth and breakage phenomena in agitated wet granulation processes: a review. Powder technology **117**(1-2), 3–39 (2001)

[3] Mani, R., Kadau, D., Herrmann, H.J.: Liquid migration in sheared unsaturated granular media. Granular Matter **15**(4), 447–454 (2013)

[4] Khamseh, S., Roux, J.-N., Chevoir, F.: Flow of wet granular materials: A numerical study. Physical Review E **92**(2), 022201 (2015)

[5] Louati, H., Oulahna, D., Ryck, A.: Apparent friction and cohesion of a partially wet granular material in steady-state shear. Powder Technology **278**, 65–71 (2015)

[6] Berger, N., Azéma, E., Douce, J.-F., Radjai, F.: Scaling behaviour of cohesive granular flows. EPL (Europhysics Letters) **112**(6), 64004 (2016)

[7] Richefeu, V., El Youssoufi, M.S., Radjai, F.: Shear strength properties of wet granular materials. Physical Review E **73**(5), 051304 (2006)

[8] Singh, A., Magnanimo, V., Saitoh, K., Luding, S.: Effect of cohesion on shear banding in quasistatic granular materials. Physical Review E **90**(2), 022202 (2014)

[9] Vo, T.T., Nezamabadi, S., Mutabaruka, P., Delenne, J.-Y., Radjai, F.: Additive rheology of complex granular flows. Nature communications **11**(1), 1–8 (2020)

[10] Roy, S., Luding, S., Weinhart, T.: A general (ized) local rheology for wet granular materials. New journal of physics **19**(4), 043014 (2017)

[11] Gans, A., Pouliquen, O., Nicolas, M.: Cohesion-controlled granular material. Phys. Rev. E **101**(3), 032904 (2020)

[12] Abramian, A., Staron, L., Lagrée, P.-Y.: The slumping of a cohesive granular column: Continuum and discrete modeling. J. Rheol. **64**(5), 1227–1235 (2020)

[13] Awdi, A., Chateau, C., Chevoir, F., Roux, J.-N., Fall, A.: Viscous dissipation in large amplitude oscillatory shear of unsaturated wet granular matter. Journal of Rheology **67**(2), 365–372 (2023)

[14] Mitarai, N., Nakanishi, H.: Simple model for wet granular materials with liquid clusters. EPL (Europhysics Letters) **88**(6), 64001 (2010)

[15] Scheel, M., Seemann, R., Brinkmann, M., Di Michiel, M., Sheppard, A., Breidenbach, B., Herminghaus, S.: Morphological clues to wet granular pile stability. Nature materials **7**(3), 189–193 (2008)

[16] Pakpour, M., Habibi, M., Møller, P., Bonn, D.: How to construct the perfect sandcastle. Scientific reports **2**(1), 1–3 (2012)

[17] Bocquet, L., Charlaix, E., Restagno, F.: Physique des materiaux granulaires humides. Comptes rendus-Physique **2**(3), 207–215 (2002)

[18] Iveson, S.M., Beathe, J.A., Page, N.W.: The dynamic strength of partially saturated powder compacts: the effect of liquid properties. Powder Technology **127**(2),

149–161 (2002)

[19] Ehrichs, E., Jaeger, H., Karczmar, G.S., Knight, J.B., Kuperman, V.Y., Nagel, S.R.: Granular convection observed by magnetic resonance imaging. Science **267**(5204), 1632–1634 (1995)

[20] Ovarlez, G., Bertrand, F., Rodts, S.: Local determination of the constitutive law of a dense suspension of noncolloidal particles through magnetic resonance imaging. Journal of rheology **50**(3), 259–292 (2006)

[21] Bonn, D., Rodts, S., Groenink, M., Rafai, S., Shahidzadeh-Bonn, N., Coussot, P.: Some applications of magnetic resonance imaging in fluid mechanics: complex flows and complex fluids. Annu. Rev. Fluid Mech. **40**, 209–233 (2008)

[22] Coussot, P.: Progress in rheology and hydrodynamics allowed by nmr or mri techniques. Experiments in Fluids **61**, 1–20 (2020)

[23] Bonamy, D., Daviaud, F., Laurent, L.: Experimental study of granular surface flows via a fast camera: a continuous description. Physics of fluids **14**(5), 1666–1673 (2002)

[24] Jarray, A., Magnanimo, V., Luding, S.: Wet granular flow control through liquid induced cohesion. Powder technology **341**, 126–139 (2019)

[25] Liao, C.-C., Hsiau, S.-S.: Influence of interstitial fluid viscosity on transport phenomenon in sheared granular materials. Chemical Engineering Science **64**(11), 2562–2569 (2009)

[26] Deboeuf, S., Lenoir, N., Hautemayou, D., Bornert, M., Blanc, F., Ovarlez, G.: Imaging non-brownian particle suspensions with x-ray tomography: Application to the microstructure of newtonian and viscoplastic suspensions. Journal of Rheology **62**(2), 643–663 (2018)

[27] Badetti, M., Fall, A., Hautemayou, D., Chevoir, F., Aimedieu, P., Rodts, S., Roux, J.-N.: Rheology and microstructure of unsaturated granular materials: Experiments and simulations. J. Rheol. **1175**, 1175–1186 (2018)

[28] Karmakar, S.: Experimental investigations of mechanical properties of wet granular materials. PhD thesis, Saarland University, Saarbrücken, Germany (2014)

[29] Manahiloh, K.N., Meehan, C.: Determining the soil water characteristic curve and interfacial contact angle from microstructural analysis of x-ray ct images. Journal of Geotechnical and Geoenvironmental Engineering **143**, 04017034 (2017) https://doi.org/10.1061/(ASCE)GT.1943-5606.0001677

[30] Milatz, M., Hüsener, N., Viggiani, G.C., Andò, E., Grabe, J.: Quantitative

3D imaging of partially saturated granular materials under uniaxial compression. Acta Geotechnica **16**, 3573–3600 (2021) https://doi.org/10.1007/s11440-021-01315-5

[31] Milatz, M., Andò, E., Viggiani, G.C., Mora, S.: In situ X-ray CT imaging of transient water retention experiments with cyclic drainage and imbibition. Open Geomechanics **3**, 1–33 (2022) https://doi.org/10.5802/ogeo.13

[32] Kido, R., Higo, Y.: Microscopic characteristics of partially saturated dense sand and their link to macroscopic responses under triaxial compression conditions. Acta Geotechnica **15**(11), 3055–3073 (2020) https://doi.org/10.1007/s11440-020-01049-w

[33] Mani, R., Kadau, D., Or, D., Herrmann, H.J.: Fluid depletion in shear bands. Physical review letters **109**(24), 248001 (2012)

[34] Amarsid, L., Awdi, A., Fall, A., Roux, J.-N., Chevoir, F.: Viscous effects in sheared unsaturated wet granular materials. Journal of Rheology **68**(4), 523–537 (2024)

[35] Fall, A., Ovarlez, G., Hautemayou, D., Mézière, C., Roux, J.-N., Chevoir, F.: Dry granular flows: Rheological measurements of the μ (i)-rheology. Journal of rheology **59**(4), 1065–1080 (2015)

[36] Badetti, M., Fall, A., Chevoir, F., Roux, J.-N.: Shear strength of wet granular materials: macroscopic cohesion and effective stress – discrete numerical simulations, confronted to experimental measurements. Eur. Phys. J. E **41**(5), 68 (2018)

[37] MiDi, G.: On dense granular flows. The European Physical Journal E **14**(4), 341–365 (2004)

[38] Da Cruz, F., Emam, S., Prochnow, M., Roux, J.-N., Chevoir, F.: Rheophysics of dense granular materials: Discrete simulation of plane shear flows. Physical Review E **72**(2), 021309 (2005)

[39] Badran, A., Marshall, D., Legault, Z., Makovetsky, R., Provencher, B., Piché, N., March, M.: Automated segmentation of computed tomography images of fiber-reinforced composites by deep learning. Journal of Materials Science **55**, 16273–16289 (2020)

[40] Iglesias, J.C., Santos, R.B.M., Paciornik, S.: Deep learning discrimination of quartz and resin in optical microscopy images of minerals. Minerals Engineering **138**, 79–85 (2019)

[41] Lorenzoni, R., Curosu, I., Léonard, F., Paciornik, S., Mechtcherine, V., Silva,

F.A., Bruno, G.: Combined mechanical and 3d-microstructural analysis of strain-hardening cement-based composites (shcc) by in-situ x-ray microtomography. Cement and Concrete Research **136**, 106139 (2020)

[42] Breiman, L.: Random forests. Machine Learning **45**, 5–32 (2001)

[43] Ronneberger, O., Fischer, P., Brox, T.: U-net: Convolutional networks for biomedical image segmentation. In: Navab, N., Hornegger, J., Wells, W.M., Frangi, A.F. (eds.) Medical Image Computing and Computer-Assisted Intervention – MICCAI 2015, pp. 234–241. Springer, Cham (2015)

[44] Dragonfly 2022.1 [Computer software]. Comet Technologies Canada Inc., Montreal, Canada (2022). https://dragonfly.comet.tech

[45] Rizzo, R.E., Freitas, D., Gilgannon, J., Seth, S., Butler, I.B., McGill, G.E., Fusseis, F.: Using internal standards in time-resolved X-ray micro-computed tomography to quantify grain-scale developments in solid-state mineral reactions (2024). https://doi.org/10.5194/se-15-493-2024

[46] Wernersson, E.L.G., Boone, M.N., Bulcke, J.V., Hoorebeke, L.V., Hendriks, C.L.L.: Postprocessing method for reducing phase effects in reconstructed microcomputed-tomography data. J. Opt. Soc. Am. A **30**(3), 455–461 (2013) https://doi.org/10.1364/JOSAA.30.000455

[47] Scheel, M.: Experimental investigations of the mechanical properties of wet granular matter. PhD thesis, Georg-August-University Göttingen (2010). https://doi.org/10.53846/goediss-2677

[48] Hamwood, J., Alonso-Caneiro, D., Read, S.A., *et al.*: Effect of patch size and network architecture on a convolutional neural network approach for automatic segmentation of oct retinal layers. Biomed Opt Express **9**, 3049 (2018)

[49] Sudre, C.H., Li, W., Vercauteren, T., *et al.*: Generalised dice overlap as a deep learning loss function for highly unbalanced segmentations. In: Deep Learning in Medical Image Analysis and Multimodal Learning for Clinical Decision Support, pp. 240–248. Springer, Cham (2017)

[50] Taha, A.A., Hanbury, A.: Metrics for evaluating 3d medical image segmentation: analysis, selection, and tool. BMC Medical Imaging **15** (2015)

[51] Geron, A.: Hands-on machine learning with Scikit-Learn, Keras, and TensorFlow: concepts, tools, and techniques to build intelligent systems. O'Rilly, Sebastopol (2019)

[52] Optimizers - Keras Documentation. https://keras.io/api/optimizers/adadelta/. Accessed: 2 November 2023 (2023)

[53] Li-Baboud, Y.-S., Cardone, A., Chalfoun, J., Bajcsy, P., Elliott, J.: Understanding impact of image quality on segmentation accuracy. SPIE Newsroom (2013)

[54] Abdallah, Y.: Compaction banding in high-porosity limestones : Experimental observations and modelling. PhD thesis, Université Paris-Est (2019)

[55] Andò, E., Hall, S.A., Viggiani, G.C., Desrues, J., Bésuelle, P.: Experimental micromechanics: grain-scale observation of sand deformation. Géotechnique Letters **2**(3), 107–112 (2012) https://doi.org/10.1680/geolett.12.00027

[56] Andò, E., Viggiani, G.C., Hall, S.A., Desrues, J.: Experimental micro-mechanics of granular media studied by x-ray tomography: recent results and challenges. Géotechnique Letters **3**(3), 142–146 (2013) https://doi.org/10.1680/geolett.13.00036

[57] Silvani, C., Réthoré, J., Nicaise, S.: Measuring coarse grain deformation by digital image correlation. Strain, 1–16 (2021) https://doi.org/10.1111/str.12378

[58] Hall, S., Bornert, M., Desrues, J., Pannier, Y., Lenoir, N., Viggiani, G.C., Bésuelle, P.: Discrete and continuum analysis of localised deformation in sand using x-ray μct and volumetric digital image correlation. Géotechnique **60**(5), 315–322 (2010)

[59] Walt, S., Schönberger, J.L., Nunez-Iglesias, J., Boulogne, F., Warner, J.D., Yager, N., Gouillart, E., Yu, T., contributors: scikit-image: image processing in Python. PeerJ **2**, 453 (2014) https://doi.org/10.7717/peerj.453

[60] Lorensen, W.E., Cline, H.E.: Marching cubes: A high resolution 3d surface construction algorithm. In: Proceedings of the 14th Annual Conference on Computer Graphics and Interactive Techniques, pp. 163–169. Association for Computing Machinery, ??? (1987). https://doi.org/10.1145/37401.37422 . https://doi.org/10.1145/37401.37422

[61] Lindblad, J.: Surface area estimation of digitized 3d objects using weighted local configurations. Image and Vision Computing **23**(2), 111–122 (2005) https://doi.org/10.1016/j.imavis.2004.06.012 . Discrete Geometry for Computer Imagery

[62] Wadell, H.: Volume, shape, and roundness of quartz particles. The Journal of Geology **43**, 250–280 (1935)

[63] Yildirim, B., Brown, H.G.: By256/rdfpy: Rdfpy-v1.0.0. https://doi.org/10.5281/zenodo.4625675 . https://doi.org/10.5281/zenodo.4625675

[64] Torquato, S., Haslach Jr, H.W.: Random heterogeneous materials: microstructure and macroscopic properties. Appl. Mech. Rev. **55**(4), 62–63 (2002)

[65] Torquato, S., Truskett, T.M., Debenedetti, P.G.: Is random close packing of

spheres well defined? Physical review letters **84**(10), 2064 (2000)

[66] Aste, T., Saadatfar, M., Senden, T.J.: The geometrical structure of disordered sphere packings. Physical Review E **71**, 061302 (2005)

[67] Agnolin, I., Roux, J.-N.: Internal states of model isotropic granular packings. I. Assembling process, geometry, and contact networks. Physical Review E **76**(6), 061302 (2007)

[68] Camenen, J.-F., Descantes, Y., Richard, P.: Effect of confinement on dense packings of rigid frictionless spheres and polyhedra. Physical Review E **86**(6), 061317 (2012)

[69] Chambolle, A.: An algorithm for total variation minimization and applications. Journal of Mathematical Imaging and Vision **20**, 89–97 (2004)